JOURNAL OF PROPULSION AND POWER
Vol. 20, No. 5, September–October 2004

Numerical Simulation of Hot Gas Nozzle Flows

A. Gross*
University of Arizona, Tucson, Arizona 85721
and
C. Weiland†
European Aeronautic Defence and Space Company, 81663 Munich, Germany

A numerical method for the simulation of hot gas nozzle flows is explained. This method solves the Reynolds-averaged Navier–Stokes equations in a finite volume context. Numerical simulations of the Vulcain and Vulcain 2 separated nozzle flows are presented. For these simulations, three different gas models were used: The gas was assumed to be either a) a perfect gas, b) in chemical equilibrium, or c) in chemical nonequilibrium. Comparisons with experimental data are provided. Free-shock separation, restricted-shock separation and cap-shock patterns are discussed. Postcombustion in the shear layer where the hydrogen-rich nozzle gas mixes with the ambient air is investigated.

Nomenclature

C, s, A	=	Arrhenius equation constants
c	=	sound speed, mass fraction
c_F	=	skin friction coefficient
c_p, c_v	=	specific heats
$\mathcal{D}$	=	diffusion coefficient
e	=	total energy
$\boldsymbol{F}$	=	flux vector
h	=	enthalpy
J	=	cell volume
k	=	turbulence kinetic energy, reaction rate constant
Le	=	Lewis number
M	=	Mach number
$\mathcal{M}$	=	mole mass
O/F	=	oxidizer/fuel mixture ratio
P_k	=	turbulence kinetic energy production term
Pr	=	Prandtl number
p	=	static pressure
$\boldsymbol{Q}$	=	state vector
Re	=	Reynolds number
r	=	radius
$\boldsymbol{S}$	=	source term vector
Sc	=	Schmidt number
T	=	temperature
t	=	time
V	=	contravariant velocity
v	=	velocity
$\dot{w}$	=	species rate of change
X	=	mole fraction
$[X]$	=	species concentration
x	=	physical coordinate
α, β	=	turbulence model constants
γ	=	ratio of specific heats
ε	=	internal energy
κ	=	thermal conductivity
μ	=	viscosity
ν	=	stoichiometric mole numbers
ξ	=	transformed coordinate
ρ	=	density
σ^*	=	turbulence model constant
τ	=	stress
ω	=	turbulence dissipation

Subscripts

a	=	ambient state
b	=	backward
cl	=	centerline
c	=	combustion chamber
f	=	forward
i, j, k	=	direction, species
$,i$	=	derivative in x_i direction
r	=	reaction
S	=	species
T	=	turbulence
th	=	nozzle throat
w	=	wall

Superscript

v	=	viscous

Received 4 September 2003; revision received 2 February 2004; accepted for publication 2 February 2004.

*Postdoctoral Student, Aerospace and Mechanical Engineering Department, 1130 North Mountain Avenue; agross@email.arizona.edu.

†Manager, P.O. Box 801186; claus.weiland@space.eads.net. Member AIAA.

Introduction

DURING the design phase of new rocket engine nozzles, extensive test campaigns have to be performed to clarify open design questions. These tests (Fig. 1) can be very costly and time consuming. However, only the full-scale test of a new design under realistic conditions can provide the final confidence required for the acceptance of new flight hardware. Nevertheless, a reduction of the amount of testing is desirable from an economical point of view.

The physical understanding of the behavior of nozzle flows has dramatically increased in the last decade, in part due to the successful application of numerical simulation methods. These prediction methods can aid in the interpretation of test data and may be used to make cautious interpolations between experimental data. Thus, they help in the design process of new rocket engine nozzles and may reduce the number of tests required. Furthermore, they can be used to study certain aspects of nozzle flows selectively by taking out different levels of flow complexity, for example, combustion or time accuracy.

During operation, mechanical and thermal loads affect the nozzle structure and lead to its deformation. The combustion is unsteady and turbulent. Fuel and oxidizer may exist in droplet form before they evaporate and burn in a bright flame, emitting radiation. The

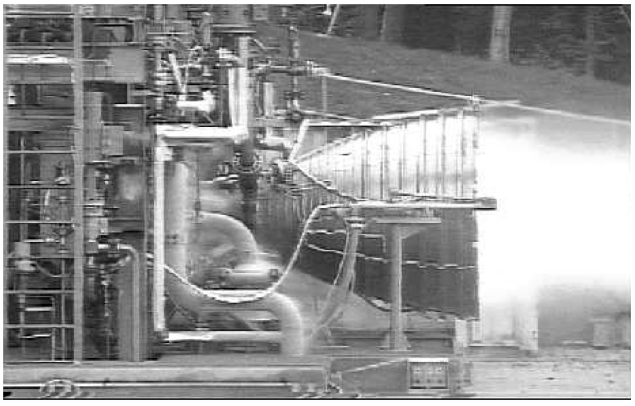

Fig. 1 Vulcain test at DLR.

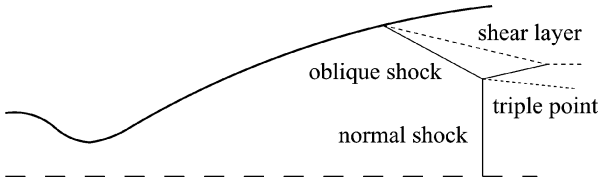

Fig. 2 Schematic view of FSS.

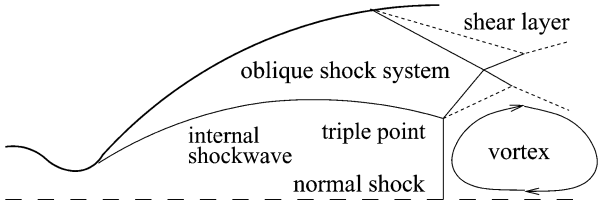

Fig. 3 Schematic view of cap-shock pattern in a parabolic nozzle.

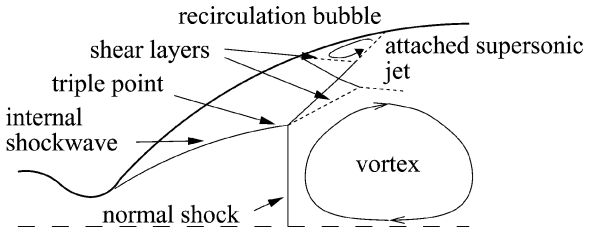

Fig. 4 Schematic view of RSS.

gas molecules may be vibrationally and rotationally excited, dissociated, or ionized. The nozzle surface can be catalytic. The flow is not axisymmetric, which is also valid for the separation line ("teepee" pattern[1]), and is violently unsteady.

Because of the great number of physical phenomena involved, flow simulations become very challenging or impossible if all relevant mechanisms and scales have to be included and resolved. The introduction of models reduces the computational requirement. Structural models, turbulence models, and combustion models, among others, are generally unavoidable when full-scale hot gas nozzle flows are considered. Because no model is universal, and the model assumptions are usually valid for only a number of test cases, their validity and applicability should be reevaluated for every new application. One of the many decisions that have to be made before hot gas nozzle flows are simulated is how complex the gas model shall be.

The classical shock pattern known for separated nozzle flows is shown in Fig. 2. In thrust optimized parabolic nozzles, an internal shock wave originating from the nozzle throat can interact with the normal shock and cause the appearance of the cap-shock pattern (Fig. 3). Depending on the flow momentum balance[2] the flow can

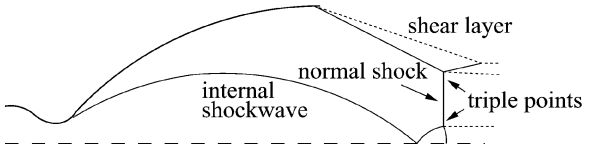

Fig. 5 Schematic view of FSS with Mach disk in a parabolic nozzle.

separate from the wall without reattaching to it [free-shock separation (FSS)] or with reattaching to it [restricted shock separation (RSS), Fig. 4]. If the normal shock crosses the nozzle centerline downstream of the reflection point of the internal shock wave at the axis (Fig. 5), the shock pattern resembles that of the classical Mach disk (Fig. 2). For RSS, the reattaching boundary layer, having passed through the oblique shocks associated with boundary-layer separation and reattachment, is very hot and exposes the nozzle wall downstream of the recirculation bubble to large thermal loads.

It is not fully understood why the nozzle wall is also subjected to large heat loads in case of FSS. The oblique shock associated with flow separation is responsible for the high pressure and temperature of the separated supersonic flow. The outer region of this separated flow encounters violent turbulent mixing with entrained ambient air, possibly causing post-combustion. If the flow separates inside the nozzle, and the pressure ratio is held constant, the wall downstream of the separation may be exposed to thermal loads high enough to make the nozzle material glow. The mechanisms responsible for the transport of the hot gases to the wall are not well understood. The highly turbulent, three-dimensional, and unsteady nature of the flow may offer an explanation. If the flow was steady and axisymmetric, entrained cool ambient air would flow alongside the nozzle wall and cool it. Gas radiation from the postcombustion zone is not strong enough to serve as an explanation for the wall heat loads observed in the experiment.

Earlier numerical simulations of separated nozzle flows do mostly assume that the gas is perfect. Chen at al. presented numerical simulations of a scaled down J-2 nozzle using the perfect-gas equation and the Baldwin–Lomax turbulence model (see Ref. 3). The simulations showed FSS during startup and RSS during shutdown. A somewhat coarsely resolved simulation of the Vulcain nozzle with a shock-capturing method showed RSS for Vulcain.[4] Experimental and numerical results for the Volvo Aero Corporation (VAC) S1 subscale nozzle were given by Mattsson et al.[5] Hunter presented results for another cold gas subscale nozzle.[6] He managed to achieve excellent flow separation location predictions with a two-equation explicit algebraic stress model. However, the nozzle he chose did not feature RSS. A simulation of the space shuttle main engine (SSME) nozzle with finite rate hydrogen/oxygen/air chemistry was performed by Dougherty and Liu.[7] A set of 25 reactions with full H_2/O_2 chemistry and N_2, N, and NO species was considered. The focus was on the interaction of the nozzle plume with the freestream.

For the results presented in this paper the, European Aeronautic Defence and Space Company (EADS-ST) Reynolds-averaged Navier–Stokes (RANS) finite volume code DAVIS-VOL[8–9] was used. An earlier version of the same code was previously used for a calculation of a fully attached film-cooled nozzle flow with H_2/O_2 chemistry and 13-reactions mechanism.[9] For the present results, the reaction mechanism and constants were kept unchanged. Inert nitrogen N_2 was added to the 6-species model. The code was modified to allow for the simulation of the ambient flowfield. To improve numerical stability, new numerical schemes for discretization of the convective flux differences were added. Also, the flux differences in the circumferential direction were replaced by source terms. The results presented in this paper are for the Vulcain[10] and Vulcain 2 (Ref. 11) rocket engine nozzles. The influence of the complexity of the gas model on the resulting separation shock pattern and the wall heat loads was studied. The gas was treated as either a) a calorically perfect gas with adopted ratio of specific heats γ, b) a gas mixture in chemical equilibrium ("mixed is burnt"), or c) a chemically reacting mixture of perfect gases (finite rate chemistry, chemical nonequilibrium).

Numerical Method

Governing Equations

The governing equations in conservative form were solved in curvilinear coordinates. In the following, repeated indices indicate summations (Einstein notation). The general form of the Navier–Stokes, turbulence, and species transport equations is

$$J\frac{\partial \boldsymbol{Q}}{\partial t}+\frac{\partial \boldsymbol{F}_i}{\partial \xi_i}=\frac{1}{Re}\frac{\partial \boldsymbol{F}_i^v}{\partial \xi_i}+J\boldsymbol{S} \tag{1}$$

with state vector $\boldsymbol{Q}$, convective ($\boldsymbol{F}$) and viscous ($\boldsymbol{F}^v$) flux vectors, and source term vector $\boldsymbol{S}$. J is the cell volume and Re is the Reynolds number.

Navier–Stokes Equations

For the Navier–Stokes equations,

$$\boldsymbol{Q}=[\rho \quad \rho v_1 \quad \rho v_2 \quad \rho v_3 \quad \rho e]^T \tag{2}$$

$$\boldsymbol{F}_i=\begin{bmatrix}\rho V_i\\ \rho v_1 V_i+\xi_{i,1}p\\ \rho v_2 V_i+\xi_{i,2}p\\ \rho v_3 V_i+\xi_{i,3}p\\ (\rho e+p)V_i\end{bmatrix} \tag{3}$$

$$\boldsymbol{F}_i^v=\begin{bmatrix}0\\ f_{1i}\\ f_{2i}\\ f_{3i}\\ v_j f_{ji}+\kappa^*\xi_{i,j}T_{,j}+\mu^*\xi_{i,j}k_{,j}\end{bmatrix} \tag{4}$$

with

$$f_{ji}=\xi_{i,k}\tau_{jk} \tag{5}$$

$$\kappa^*=\kappa\left(1+\frac{\mathrm{Pr}}{\mathrm{Pr}_T}\frac{\mu_T}{\mu}\right) \tag{6}$$

$$\mu^*=\mu\left(1+\sigma^*\frac{\mu_T}{\mu}\right) \tag{7}$$

where τ_{jk} ($j,k:=x,y,z$) are shear and normal stresses. $T_{,j}$ and $k_{,j}$ are partial derivatives of temperature and turbulence kinetic energy in the j direction. Pr is the Prandtl number and $\sigma^*=0.5$ is a turbulence model constant. The source term

$$\boldsymbol{S}=\frac{1}{r}\left[0 \quad 0 \quad 0 \quad p-\frac{1}{Re}(\mu+\mu_T)\frac{v_3}{r}+\frac{2}{3}\rho k 0\right]^T \tag{8}$$

is dependent on the local distance from the centerline r and was derived under the assumption of axial symmetry and thin-layer viscous terms in the circumferential direction. It replaces the convective and viscous flux differences in the circumferential direction.[12] The contravariant velocity V_i is

$$V_i=\xi_{i,j}v_j \tag{9}$$

Turbulence Model Equations

For RANS simulations, the standard 1988 two-equation k–ω model of Wilcox[13] was used. The turbulence model state vector, convective and viscous fluxes, and the source term are

$$\boldsymbol{Q}_T=[\rho k \quad \rho\omega]^T \tag{10}$$

$$\boldsymbol{F}_{iT}=\begin{bmatrix}\rho k V_i\\ \rho\omega V_i\end{bmatrix} \tag{11}$$

$$\boldsymbol{F}_{iT}^v=\left(\mu+\sigma^*\mu_T\right)\begin{bmatrix}\xi_{i,j}k_{,j}\\ \xi_{i,j}\omega_{,j}\end{bmatrix} \tag{12}$$

$$S_T=\begin{bmatrix}P_k-Re\beta^*\rho k\omega\\ \alpha\dfrac{\rho}{\mu_T}P_k-Re\beta\rho\omega^2\end{bmatrix} \tag{13}$$

The k production term is based on the Boussinesq approximation for the Reynolds stresses

$$P_k=(1/Re)\tau_{ij}v_{i,j} \tag{14}$$

The eddy viscosity becomes

$$\mu_T=\rho k/\omega \tag{15}$$

Wilcox's compressible dissipation was used to dampen the turbulence production.[14] Here, the model constants are modified

$$\beta_{\mathrm{corr}}=\beta\left[1-\tfrac{6}{5}\alpha_T F(M_T)\right] \tag{16}$$

$$\beta^*_{\mathrm{corr}}=\beta^*[1+\alpha_T F(M_T)] \tag{17}$$

$$F(M_T)=\left(M_T^2-M_{T0}^2\right)H(M_T-M_{T0}) \tag{18}$$

where $M_T=\sqrt{(2k/c^2)}$ is the turbulence Mach number, and $H(\,)$ is the Heaviside function.

Species Transport Equations

If finite rate chemistry is considered, additional transport equations have to be solved.[9,15] The state vector, convective, and viscous flux vectors are

$$\boldsymbol{Q}_S=\rho[c_1 \quad c_2 \quad \cdots]^T \tag{19}$$

$$\boldsymbol{F}_{iS}=\rho\begin{bmatrix}c_1 V_i\\ c_2 V_i\\ \cdots\end{bmatrix} \tag{20}$$

$$\boldsymbol{F}_{iS}^v=\frac{\rho}{Sc}\begin{bmatrix}\mathcal{D}_1^*\xi_{i,j}c_{1,j}\\ \mathcal{D}_2^*\xi_{i,j}c_{2,j}\\ \cdots\end{bmatrix} \tag{21}$$

with Schmidt number $Sc(Sc=Pr/Le)$ and diffusion constant

$$\mathcal{D}_k^*=\mathcal{D}_k+(Sc/Sc_T)(\mu_T/\rho) \tag{22}$$

The species molecular weight $\mathcal{M}_k$ relates the species mass fraction $c_k=\rho_k/\rho$ ($\sum c_k=1$) to the species mole fraction

$$X_k=(\mathcal{M}/\mathcal{M}_k)c_k \tag{23}$$

and the species concentration

$$[X_k]=\rho_k/\mathcal{M}_k \tag{24}$$

The mixtures molecular weight is obtained from $\mathcal{M}=1/(\sum c_k/\mathcal{M}_k)$. The source term is

$$\boldsymbol{S}_S=[\dot{w}_1 \quad \dot{w}_2 \quad \cdots]^T \tag{25}$$

with

$$\dot{w}_k=\mathcal{M}_k\frac{\mathrm{d}[X_k]}{\mathrm{d}t} \tag{26}$$

For a given system of reactions,

$$\sum \nu'_j X_j \rightleftharpoons \sum \nu''_l X_l \tag{27}$$

with stoichiometric mole numbers ν' and ν'', the reaction rates are

$$\frac{\mathrm{d}[X_i]}{\mathrm{d}t} = \sum_{\substack{\text{for all reactions } r \text{ that} \\ \text{species } i \text{ participates in}}} (\nu''_{i,r} - \nu'_{i,r}) \left\{ k_{f,r} \prod_{\substack{\text{all reactants } j \\ \text{involved in reaction } r}} [X_j]^{\nu'_{j,r}} - k_{b,r} \prod_{\substack{\text{all products } l \\ \text{of reaction } r}} [X_l]^{\nu''_{l,r}} \right\} \quad (28)$$

The chemical rate constants k are taken from an Arrhenius equation

$$k = CT^s e^{-A/T} \quad (29)$$

Gas Modeling

Calorically Perfect Gas

The ratio of specific heats γ is constant. Enthalpy h and internal energy ε are functions of temperature T only. For μ, a polynomial fit through data obtained from the Gordon and McBride computer program[16] (also see Ref. 17) for the given oxidizer/fuel mixture ratio O/F is used. The static pressure p is computed from the perfect-gas relation

$$p = \rho T/\gamma M^2 \quad (30)$$

The thermal conductivity is

$$\kappa = [1/(\gamma - 1)PrM^2]\mu \quad (31)$$

Gas Mixture in Chemical Equilibrium

If the mixture properties and composition varies noticeably in the temperature and pressure range of interest, the perfect-gas equation may not be accurate enough. If the mixture is in chemical equilibrium (mixed is burnt), the gas properties for a certain oxidixer/fuel ratio O/F (dependent on density ρ and internal energy ε) can be computed with the Gordon and McBride computer program[16] (also see Ref. 17) and stored in two-dimensional lookup tables. During the run time of the flow simulation program, all relevant flow quantities are interpolated from these lookup tables.

Chemically Reacting Mixture of Perfect Gases (Finite Rate Chemistry)

The term

$$(1/Sc)\mathcal{D}_k^* \rho h_k \xi_{i,j} c_{k,j} \quad (32)$$

is added to the last line of the viscous flux vector F_i^v [Eq. (4)]. The perfect-gas equation holds for each species and for the mixture. Summation of the partial pressures and densities yields the mixture pressure $p = \sum p_k$ and density $\rho = \sum \rho_k$. To compute the mixture enthalpy the individual species enthalpies h_k are weighted by the mass fractions ($h = \sum c_k h_k$). The multicomponent diffusion coefficient $\mathcal{D}_k$ is computed from the binary diffusion coefficients $\mathcal{D}_{kl}$

$$\mathcal{D}_k = \frac{1 - X_k}{\sum_l (X_l/\mathcal{D}_{kl})} \quad (33)$$

Polynomial fits are used for the species enthalpies h_k, the binary diffusion coefficients $\mathcal{D}_{kl}$, the specific heats c_p and c_v, the thermal conductivity κ, and the viscosity μ (Ref. 18). The polynomial coefficients for h_k, c_p, and c_v can be found in Refs. 16 and 17, whereas the polynomial coefficients for the diffusion coefficients $\mathcal{D}_{kl}$, κ, and μ were obtained from the earlier version of the code.[9] The Arrhenius constants can be found in Ref. 19.

For the flow simulations presented herein, seven species (O_2, H_2, OH, O, H, H_2O, and inert N_2) and 13 reactions (Table 1) were considered. Except for the addition of inert nitrogen N_2, this is the same approach as that used in Ref. 9.

Table 1 Kinetic mechanism

Mechanism	Reaction
1	$H_2 + O \rightleftharpoons OH + H$
2	$H_2O + H \rightleftharpoons H_2 + OH$
3	$H_2O + O \rightleftharpoons 2OH$
4	$O_2 + H \rightleftharpoons OH + O$
5	$H_2 + H_2 \rightleftharpoons 2H + H_2$
6	$H_2 + H_2O \rightleftharpoons 2H + H_2O$
7	$H_2 + O_2 \rightleftharpoons 2H + O_2$
8	$H_2O + H_2 \rightleftharpoons H + OH + H_2$
9	$H_2O + H_2O \rightleftharpoons H + OH + H_2O$
10	$H_2O + O_2 \rightleftharpoons H + OH + O_2$
11	$O_2 + H_2 \rightleftharpoons 2O + H_2$
12	$O_2 + H_2O \rightleftharpoons 2O + H_2O$
13	$O_2 + O_2 \rightleftharpoons 2O + O_2$

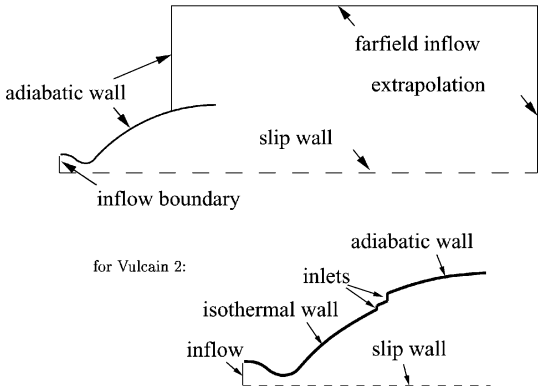

Fig. 6 Boundary conditions.

Boundary Conditions

The inflow and inlet conditions were computed with the Gordon and McBride computer program[16] (also see Ref. 17), under the assumption of a one-dimensional isentropic expansion in chemical equilibrium from the specified chamber conditions. The computed conditions were prescribed directly. The inflow Mach numbers were 0.246 for Vulcain and 0.271 for Vulcain 2. A top-hat velocity profile was used at the inflow boundary (Fig. 6) and one-seventh-velocity profiles were used at the inlets. The turbulence levels were unknown and had to be guessed.

The nozzle wall was treated as adiabatic, the only exception being the wall upstream of the first inlet for Vulcain 2. This part was treated as isothermal. The dissipation ω at the wall was set to a finite value defined by the surface roughness.[14] Walls were assumed to be hydraulically smooth and noncatalytic.[18] Neither turbulence wall functions nor wall distances were needed. The centerline was treated as a slip wall. At the outflow boundary, all flow quantities were extrapolated.

At the farfield inflow boundary, the velocities were extrapolated to the boundary for the finite rate chemistry computations. Because the velocities were small, the acceleration from the ambient state to the inflow boundary was then assumed to be isentropic. Temperature and pressure at the farfield boundary were lowered accordingly. For the other simulations, nonreflecting boundary conditions by Giles were used[20] (see Ref. 18).

When perfect-gas simulations were performed and γ was adjusted to give better simulation results for the flow inside the nozzle, the same γ had to be used for modeling of the ambient air. In the case of chemical equilibrium computations, the gas lookup tables are generated for one fixed O/F. The ambient air had to be simulated with the same O/F. Because the ambient pressure is essential for simulations of separated nozzle flows, it was set to $p_a = 1$ bar. The gas tables were defined for $T \geq 400$ K. As the ambient gas is entrained into the nozzle, it accelerates and cools down. To avoid temperatures below 400 K, the ambient temperature was set to $T_a = 700$ K. Given

Table 2 Grid resolutions

Simulation	Inside nozzle	Total
Vulcain, equilibrium	160×160	42,688
Vulcain 2, perfect gas	128×60	13,200
Vulcain 2, equilibrium	496×80	67,200
Vulcain 2, chemically reacting (fine grid)	140×92 and 32×156 and 140×220	101,072

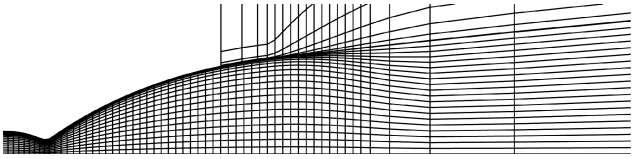

Fig. 7 Vulcain, partial view of computational grid; every fourth grid line in x and every eigth grid line in y are shown.

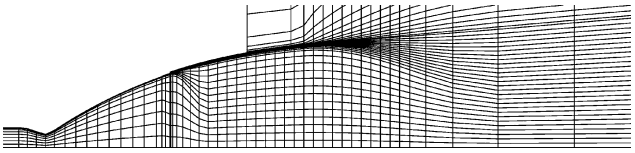

Fig. 8 Vulcain 2, finite rate chemistry computational grid; every eighth grid line is shown.

the comparatively high gas constant of the combustion gas, the ambient density at that temperature became $\rho_a = 0.287$ kg/m^3. The same p_a and T_a were also chosen for the perfect-gas simulations. No gas lookup tables were needed for the nonequilibrium computations. For these simulations, the ambient state was defined by $p_a = 1$ bar, $T_a = 350$ K, $\rho_a = 1.0$ kg/m^3, $c_{O_2} = 0.262$, and $c_{N_2} = 0.738$.

Because the gas composition at the inlets is significantly different from the nozzle core flow, the full Vulcain 2 nozzle flow can only be computed when the finite rate chemistry is considered. To allow for perfect-gas and chemical equilibrium computations, a second contour, Vulcain 2 clean, was chosen. This contour shows the same wall pressure distribution as Vulcain 2, but does not feature inlets.

Gridding

The grid resolutions used are listed in Table 2. In addition, a coarse grid (one-half of the resolution in both directions) was used to study grid dependence for the finite rate chemistry computations. All cases were computed on grids with different resolutions. The grids chosen for the computations presented in this paper are fine enough to allow for accurate predictions of the wall properties and the global shock patterns, although certain aspects of the flow, for example, the intensity of the internal shockwave, may be underpredicted. For the turbulence model used, the laminar sublayer needed to be resolved. This was achieved by keeping the nondimensional wall distance (in wall units y^+) of the wall next cell below 1.

For the Vulcain and Vulcain 2 clean computations, the computational domain was split up into two blocks (Fig. 7). For the Vulcain 2 computation, the two inlets had to be accommodated. The inlets were treated as contour steps, necessitating two additional computational blocks (Fig. 8).

The spatial extents of the computational grids used are listed in Table 3 and were chosen based on previous experience.[18,21,22] They were measured from the intersection of the nozzle exit plane with the centerline. Massive grid stretching was used in the downstream direction close to the outflow and in the radial direction close to the far-field inflow boundary.

Solver

The EADS-ST finite volume multiblock structured grid RANS code DAVIS-VOL[8,9] was used to obtain solutions of the preceding equations. An implicit Euler method was used for time integration. The Navier–Stokes convective fluxes were discretized with a second-order accurate Roe scheme[23] (for the chemical equilibrium computations), or a second-order accurate symmetric total variation diminishing (TVD) scheme[24,25] (Vulcain 2 clean perfect-gas computation, Vulcain 2 nonequilibrium computation). The turbulence fluxes were computed with a second-order accurate Mach number-based advection pressure splitting (MAPS) like discretization[26] (Vulcain chemical equilibrium computation), a second-order accurate scheme similar to the symmetric TVD scheme by Yee (see Ref. 27) (for the Vulcain 2 clean perfect-gas simulation), a first-order upwind scheme[28] (for the Vulcain 2 clean chemical equilibrium computation), or a second-order accurate Larrouturou scheme[29] (for the Vulcain 2 nonequilibrium computation). The Larrouturou scheme was also used for the species convective fluxes.[29] All viscous fluxes were discretized by second-order accurate central differences. The steady-state solution was approached iteratively by means of a Newton iteration. To this end, the system of equations was linearized with respect to the primitive variables. The linearized equations were discretized with first-order upwind schemes for the convective terms and central differences for the viscous terms. The resulting system was solved by a line Gauss–Seidel method. Because the code was not time-accurate, only steady-state solutions were sought.

Table 3 Spatial grid extent in downstream direction I, radial direction J, and upstream direction K in multiples of the nozzle exit radius

Simulation	I	J	K
Vulcain, equilibrium	18.5	4	0.5
Vulcain 2, perfect gas	5.5	4	1.2
Vulcain 2, equilibrium	18	3.5	0.4
Vulcain 2, chemically reacting	20.5	2.5	0.5

Nozzle Flow Results

Vulcain

Still photographs taken from video footage of a Vulcain test at the German Aerospace Research Center (DLR) are shown in Figs. 1 and 9. Although the image resolution is not very good, the fuzzy appearance of the flow for $p_c/p_a = 20$ and 50 is believed not to be due to the video equipment used, but to the appearance of RSS. The video observations suggest RSS for the pressure ratios 20 and 50 ($O/F = 6.0$), the cap-shock pattern for the pressure ratio 115 and $O/F = 5.8$, and a slightly deformed Mach disk for the pressure ratio 115 and $O/F = 6.8$. This conjecture was made based on the computational results shown later. The pressure ratios and O/F at which the pictures were taken are approximate.

Different from Vulcain 2, the Vulcain nozzle does not feature flow inlets anywhere else other than in the combustion chamber. As shown by Knab and Weiland[9] for an analogous nozzle flow, where the finite rate and equilibrium chemistry models gave approximately the same results, the flow in Vulcain-type nozzles may be considered to be close to equilibrium. Because the O/F is the same everywhere in the nozzle flow (not the case for Vulcain 2, where gas with different O/F is fed into the nozzle through inlets), and if the goal is not to predict thermal loads in the separated flow region at the nozzle exit, it is generally sufficient for accurate shock pattern predictions to use the equilibrium-gas model and to model the ambient air with the same O/F as the combustion gas inside the nozzle. Therefore, the equilibrium-gas assumption was made for the Vulcain computations presented in this paper. Lookup tables for an H_2/O_2 system at four different oxidizer/fuel ratios $O/F = 5.6$, 5.8, 6.0, and 6.8 were generated. The inflow conditions for the six different cases studied are listed in Table 4. The turbulence intensity at the inflow was assumed to be 5%, and the turbulent length scale was assumed to be 10% of the nozzle throat diameter. At the far-field boundary, the turbulence kinetic energy k was set to zero, and the dissipation rate ω was set to the same value as at the nozzle

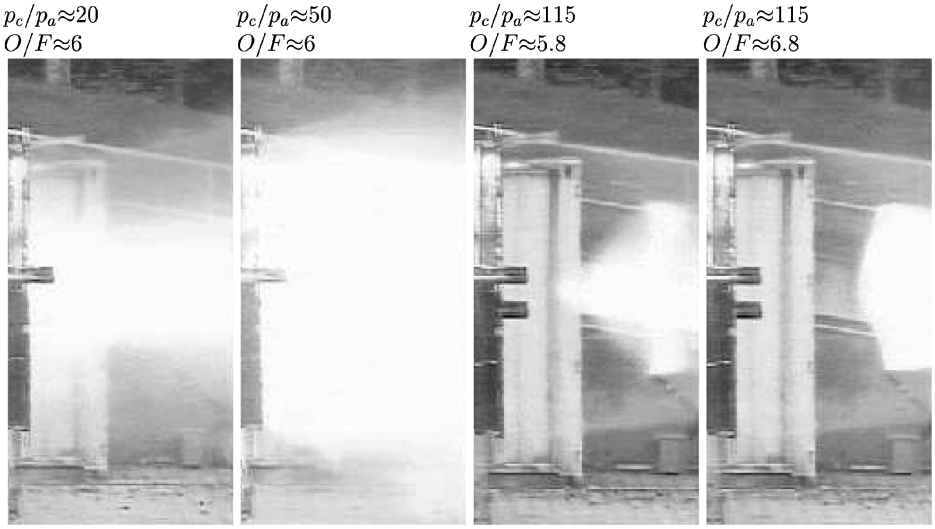

Fig. 9 Vulcain test at DLR.

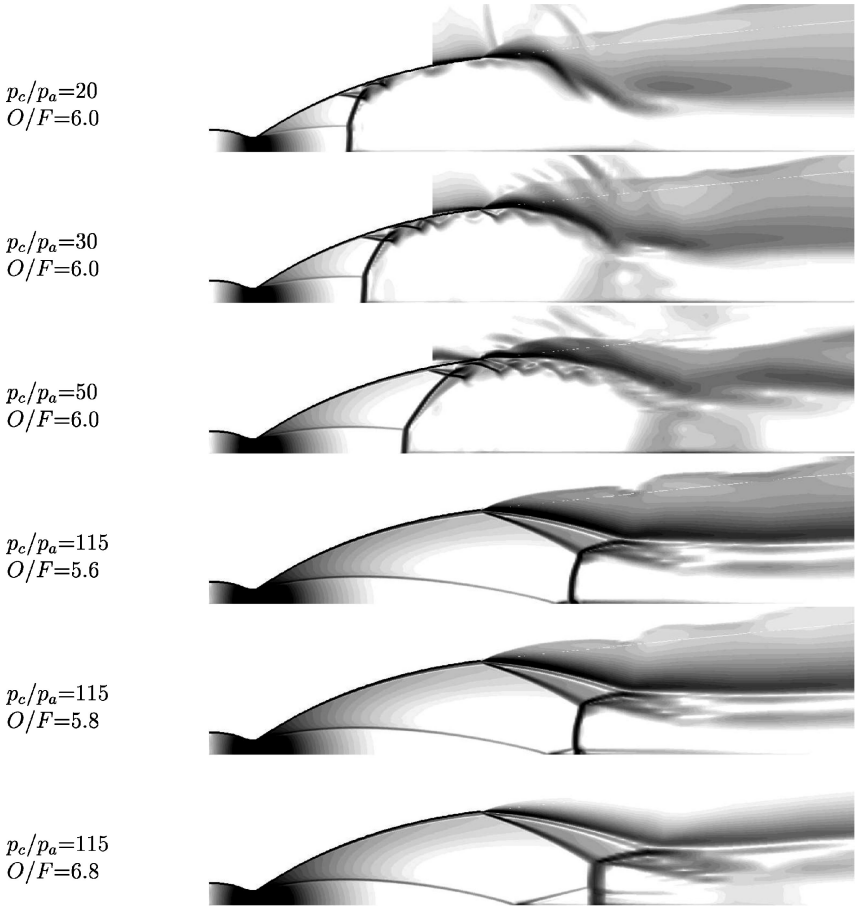

Fig. 10 Vulcain, equilibrium-gas assumption, pseudoschlieren images of computational results.

Table 4 Vulcain, equilibrium gas assumption, inflow conditions

p_c, bar	O/F	p_i, bar	T_i, K
20	6.0	19.3	3360
30	6.0	29.0	3409
50	6.0	48.3	3470
115	5.6	111.1	3496
115	5.8	111.1	3533
115	5.8	111.1	3560

inflow boundary. For the following Vulcain 2 clean computations, the same turbulence quantities were prescribed at the inflow and far-field boundaries.

For p_c/p_a =20, 30, and 50, the simulations show RSS (Fig. 10). Here, the reattached supersonic jet passes through a series of compression and rarefaction regions. This is clearly revealed by the wall pressure distributions (Fig. 11). The various oblique shocks preceding every rarefaction area are visible in the pseudoschlieren images. For $p_c/p_a = 115$, the Mach disk solution is obtained. The influence of the mixture ratio O/F on the shape of the internal shock wave becomes obvious. As O/F was lowered, the reflection point

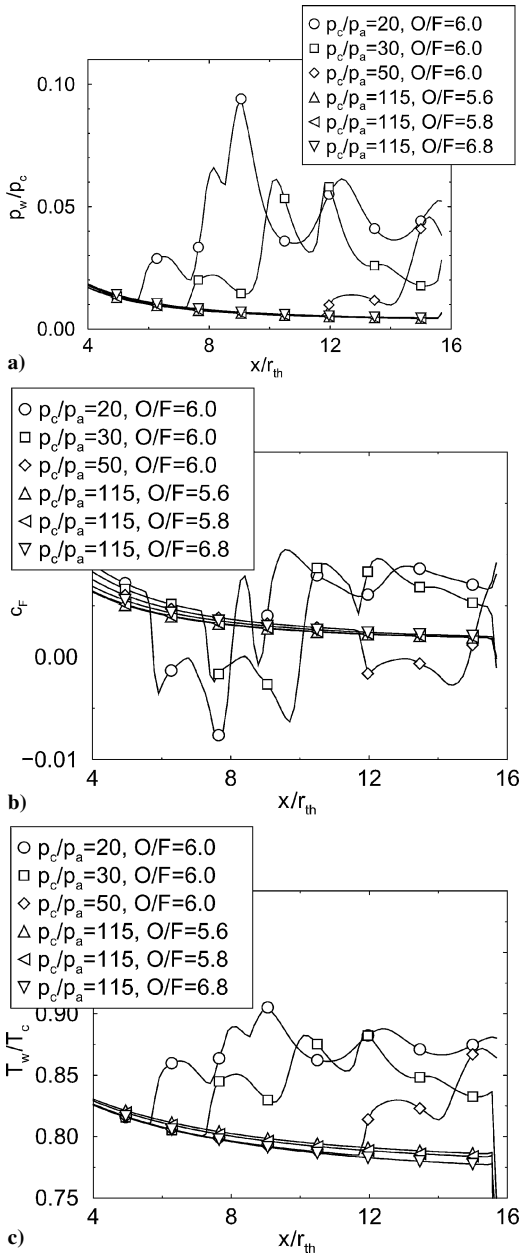

Fig. 11 Vulcain, equilibrium-gas assumption: a) wall pressure, b) skin-friction coefficient, and c) wall temperature.

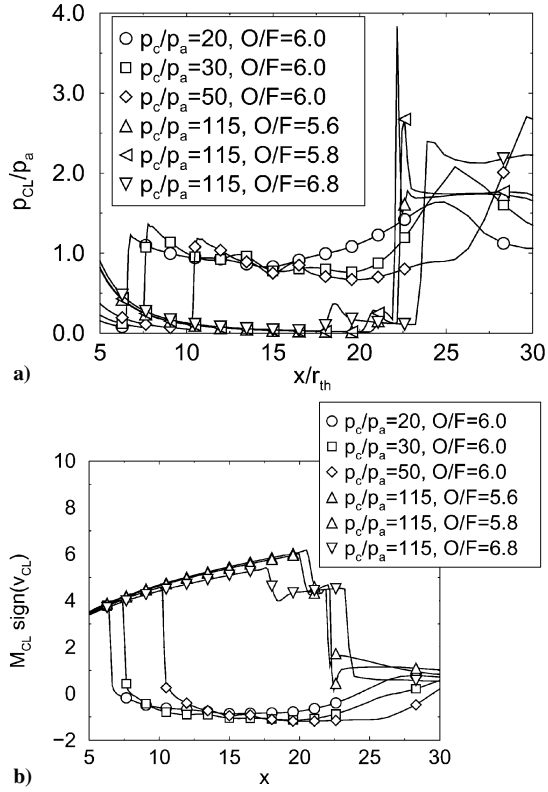

Fig. 12 Vulcain, equilibrium-gas assumption: a) centerline pressure and b) Mach number.

of the internal shock wave at the centerline moved downstream. At 5.6, the strong normal shock crosses the centerline slightly downstream of the reflection point. If O/F is lowered further, the Mach disk solution would probably transform into the cap-shock solution. However, as pointed out by Frey,[30] a hysteresis region may exist. The p_c/p_a where the transition from cap-shock pattern to Mach disk occurs during startup may be higher than the p_c/p_a where the back-transition from Mach disk to cap-shock pattern occurs during shutdown. The video images in Fig. 9 were taken during the startup phase. The $p_c/p_a = 115$ ($O/F = 5.6$) solution was obtained when O/F was lowered from the $p_c/p_a = 115$ ($O/F = 5.8$) solution.

The location and size of the enclosed separation bubble can be determined from the skin-friction distribution (Fig. 11). For all RSS cases, the wall is exposed to higher temperatures than for the full flowing cases ($p_c/p_a = 115$). Two oblique shocks can be associated with the separation bubble, a separation shock, and a reattachment shock. The reattaching supersonic jet, having passed through both shocks, is heated up considerably. Also, the boundary layer is thinner after reattachment than before separation. (Notice the higher skin-friction coefficient c_F.) Clearly, operating a nozzle in the RSS regime for a prolonged amount of time exposes the wall to high thermal loads.

The static pressure on the centerline downstream of the shock is higher for FSS ($p_{cl}/p_a \approx 2$) than for RSS ($p_{cl}/p_a \approx 1$) (Fig. 12). The reflection point of the internal shock wave at the axis appears as a sudden centerline pressure increase and a Mach number decrease. A large backflow region with centerline Mach numbers around one is positioned behind the normal shock for all RSS cases. This centerline reverse flow is the manifestation of a strong ring vortex that is located downstream of the normal shock.

A more detailed view of a typical RSS and a typical FSS solution is given in Fig. 13. Another feature of the RSS flow, a small adaptation shock, which is positioned at the nozzle exit and raises the jets static pressure to the ambient pressure level, becomes visible.

Direct comparisons with video images taken during the experiment (Fig. 9) are difficult. The visible wavelength is related to the gas temperature, and the intensity is related to the density and the temperature. According to Stefan–Boltzmann, the radiation intensity is proportional to T^4. A visualization of ρT^4 should allow for a crude comparison with the experiment (Fig. 9). Figure 14 reveals an area of low-intensity radiation filling the entire nozzle exit diameter for RSS and an area of high-intensity radiation behind the Mach disk for FSS. Based on these numerical results, the nozzle flow was assumed to be in RSS for $p_c/p_a = 50$ and FSS for $p_c/p_a = 115$.

Vulcain 2

Perfect Gas

For a fixed pressure ratio of $p_c/p_a = 115.5$, the influence of the ratio of specific heats γ on the solution was studied for the Vulcain 2 clean contour. The inflow conditions are given in Table 5. For the larger $\gamma = 1.16$, the reflection point of the internal shock wave at the centerline is further downstream. The cap-shock pattern appears (Fig. 15). For the smaller $\gamma = 1.12$, the reflection point is further upstream, and the Mach disk solution is obtained. Larger γ correspond to smaller O/F.

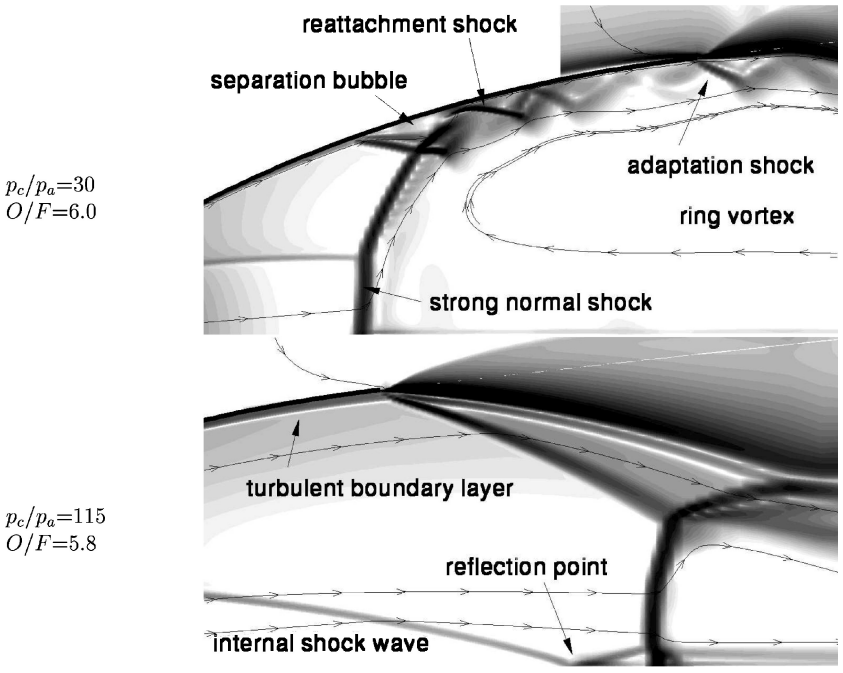

Fig. 13 Vulcain, equilibrium-gas assumption, pseudoschlieren images (close-ups).

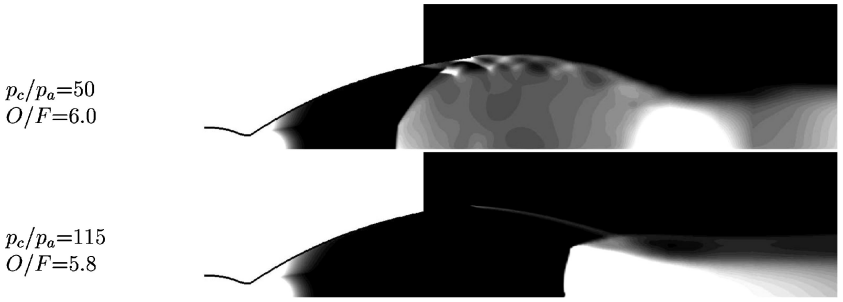

Fig. 14 Vulcain, equilibrium-gas assumption, isocontours of ρT^4.

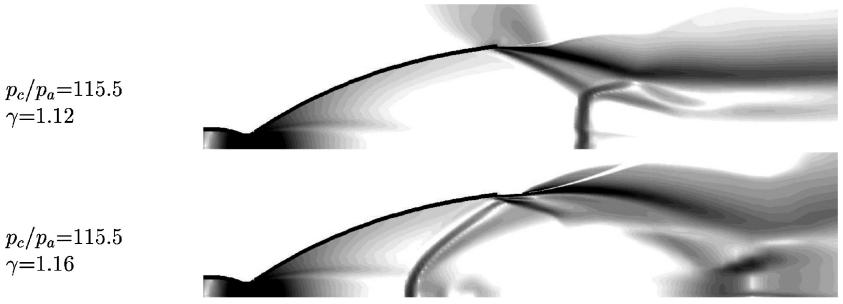

Fig. 15 Vulcain 2 clean, perfect-gas assumption, pseudoschlieren images of computational results.

Table 5 Vulcain 2 clean, perfect gas assumption, inflow conditions

p_c, bar	γ	p_i, bar	T_i, K
115.5	1.12	111.0	3669
115.5	1.16	110.8	3669

Equilibrium Gas

As mentioned earlier, the Vulcain 2 clean nozzle flow can be modeled accurately with equilibrium gas lookup tables if the interaction of the ambient gas with the combustion gas is of no interest and the ambient gas only imposes the ambient pressure. Computations were carried out for a mixture ratio $O/F = 7.2$ and three different pressure ratios (Table 6). Pseudo-schlieren images are shown in Fig. 16. At this very large O/F, the reflection point of the internal shock wave is far upstream and inside the nozzle. The Mach disk solution is obtained for all investigated pressure ratios.

A close-up at the nozzle lip is given in Fig. 17. The oblique separation shock heats up the gas to temperatures above 2200 K. With the equilibrium approach chosen for these simulations, postcombustion of remaining excess fuel with the oxygen of the ambient air cannot be simulated.

Nonequilibrium Gas

Finite rate chemistry computations at $O/F = 7.0$ were carried out for two different pressure ratios (Table 7). The inflow mass fractions were $c_{H_2} = 0.0226$, $c_{O_2} = 0.0304$, $c_{H_2O} = 0.852$, $c_{OH} = 0.0837$, $c_H = 0.00232$, $c_O = 0.00924$, and $c_{N_2} = 0$ for $p_c/p_a = 90$ and $c_{H_2} = 0.0223$, $c_{O_2} = 0.0282$, $c_{H_2O} = 0.858$, $c_{OH} = 0.0809$, $c_H = 0.00214$, $c_O = 0.00835$, and $c_{N_2} = 0$ for $p_c/p_a = 125$. The inlet conditions were $v = 1672$m/s ($M = 1$), $p = 12.7$ bar, $T = 485$ K, and $c_{H2} = 1$

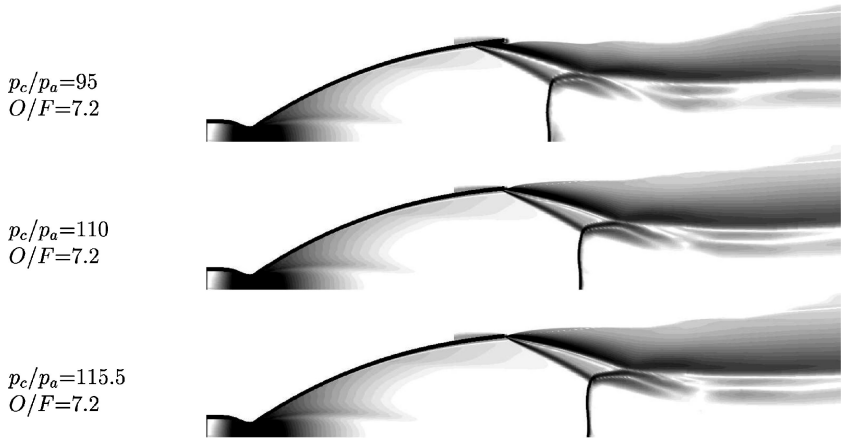

Fig. 16 Vulcain 2 clean, equilibrium-gas assumption, pseudoschlieren images of computational results.

Table 6 Vulcain 2 clean, equilibrium gas assumption, inflow conditions

p_c, bar	p_i, bar	T_i, K
95	91.2	3642
110	105.5	3662
115.5	110.8	3669

Table 7 Vulcain 2 clean, finite rate chemistry, inflow conditions

p_c, bar	p_i, bar	T_i, K
90	86.4	3626
125	119.9	3671

at the first inlet, and $v = 2112$ m/s, $p = 5.44$ bar, $T = 657$ K, $c_{H_2} = 0.464$, $c_{H_2} = 0.536$ at the second inlet. At both inlets, the fluid was injected in the wall tangential direction. These inlet conditions were kept unchanged for both pressure ratios. The inflow and inlet data were computed with the Gordon and McBride computer program[16] (see also Ref. 17) under the assumption of equilibrium chemistry and one-dimensional isentropic expansion. At the inflow boundary, the turbulence Mach number was set to 10^{-5}, and the ratio of eddy viscosity to molecular viscosity was set to 10^{-6}. The corresponding k and ω values were also prescribed at the two inlets. The inflow at the far-field boundary was considered to be laminar.

Different steps were taken to stabilize the subsonic part of the solution (because steady-state solutions were sought) and to prevent the buildup of excessive levels of turbulence in the shear layer where the nozzle jet comes into contact with the ambient air.[18] The species equations have very strong source terms and are difficult to handle numerically. This necessitates small time steps and makes nonequilibrium chemistry computations considerably more computationally expensive than equilibrium chemistry or perfect-gas simulations.

Simulation results are shown in Fig. 18. For $p_c/p_a = 90$, the flow separates noticeably upstream of the nozzle exit, and for $p_c/p_a = 125$ the flow separates approximately at the nozzle exit. The coarse grid result closely resembles the fine grid result, except for the internal shock wave, which is not well resolved. In the following, if not specified otherwise, all results are for the fine grid solutions. Isocontours of the mole fraction distributions are shown in Fig. 19. Downstream of the nozzle throat, most of the oxygen has reacted with the available hydrogen (Fig. 20) forming water H_2O. Because the fuel mixture is fuel rich, some hydrogen H_2 is left over. As the gas passes through the Mach disk it becomes heated up noticeably. The molecules crack up again, forming noteworthy amounts of H, O, and OH. The fluid films injected at the two inlets are both

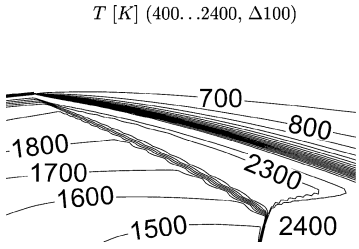

Fig. 17 Vulcain 2 clean, equilibrium-gas assumption, $p_c/p_a = 115.5$ (close-up at nozzle exit).

hydrogen-rich and cool (Fig. 21). Because the amount of left-over oxygen in the nozzle flow is close to zero, the hydrogen only burns as it comes into contact with the ambient air's oxygen (Fig. 22). The temperature distribution in the postcombustion area looks significantly different from the result obtained from the equilibrium-gas simulation (Fig. 17). Downstream of the region where the gas is heated up due to the passage through the oblique separation shock, there is a secondary temperature increase. The mole fractions of hydrogen H_2 and oxygen O_2 decrease whereas the appearance of extra water H_2O is a clear indication of postcombustion. Because the simulations are steady-state solutions, the violent turbulent mixing in the shear layer where the postcombustion takes place (Fig. 23) has to be modeled by large amounts of eddy viscosity provided by the turbulence model.

The ratio of specific heats

$$\gamma = \frac{\sum c_i c_{p_i}}{\sum c_i c_{v_i}} \tag{34}$$

is not constant (Fig. 24). The centerline γ is 1.2 in the combustion chamber and rises to a maximum of 1.25 (Fig. 25). At the reflection point of the internal shock wave at the centerline, it reaches a local minimum of 1.22. A strong discontinuity of γ can be detected downstream of the Mach disk. It may be attributed to the numerical method or to an under-resolved chain of chemical reactions. Because, apart from the smeared-out appearance of the internal shockwave, the coarse- and fine-grid results are essentially the same (Figs. 26 and 27), the grid resolution appeared to be sufficient.

Wall quantities are shown in Fig. 26. Experimental data for two circumferential locations ($\vartheta = 90$ and 270 deg) are given for $p_c/p_a = 125$. All curves are discontinuous at the inlet locations. Although the gas films generated at the inlets do initially cool down the wall by keeping the nozzle core flow at a distance, turbulent mixing at the interface of the cooling film with the nozzle core flow does eventually lead to a wall temperature increase further downstream. This temperature increase starts earlier in the experiment than in the simulation. For $p_c/p_a = 90$, the nozzle wall is exposed to high thermal loads downstream of the separation line. As the ambient air is entrained into the nozzle it oxidizes the leftover hydrogen and, thus, heats up before it comes into contact with the nozzle wall. The

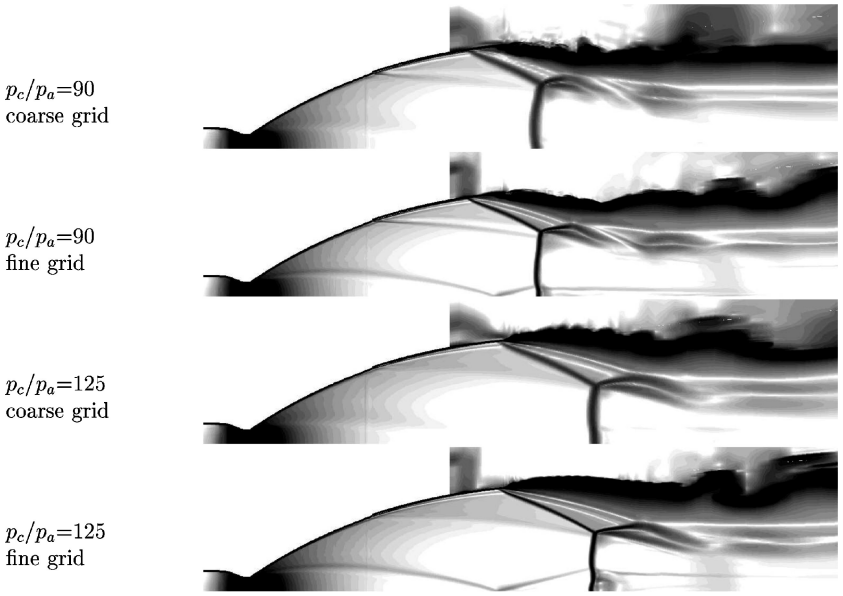

Fig. 18 Vulcain 2, finite rate chemistry, pseudoschlieren images of computational results.

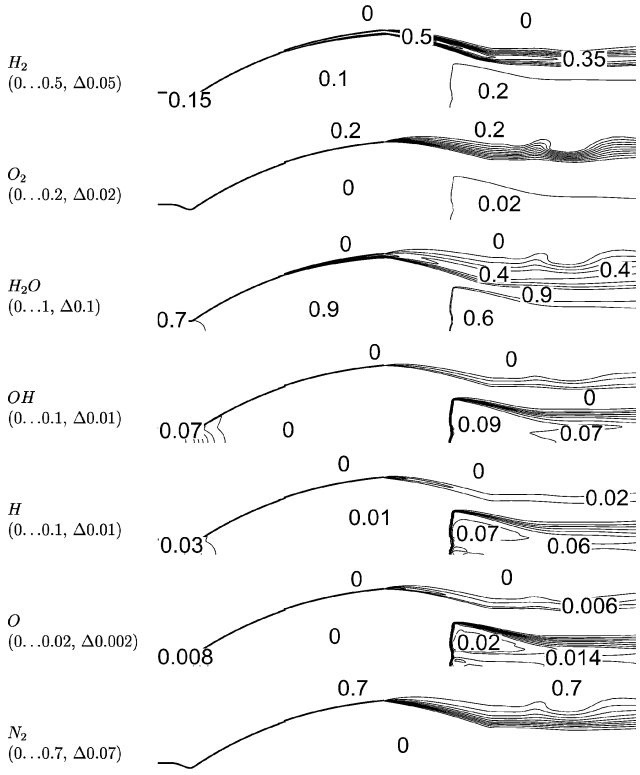

Fig. 19 Vulcain 2, finite rate chemistry, $p_c/p_a = 125$, mole fractions X.

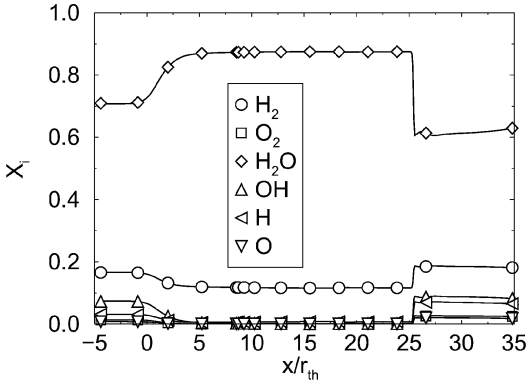

Fig. 20 Vulcain 2, finite rate chemistry, $p_c/p_a = 125$, centerline mole fractions.

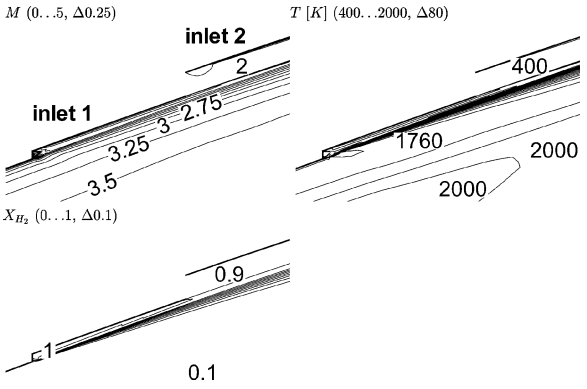

Fig. 21 Vulcain 2, finite rate chemistry, $p_c/p_a = 125$, close-ups at inlets.

turbulent diffusion provided by the turbulence model facilitates the mixing of the ambient air's oxygen with the nozzle flow's excess hydrogen. Because unsteady three-dimensional computations are still too expensive for general engineering applications, the crucial role of the turbulence model becomes obvious once again. The standard k–ω turbulence model used in the present computations does not accurately predict all of the relevant flow phenomena. It remains questionable whether all relevant aspects of hot gas nozzle flows can be simulated by numerical methods in the near future. In the meantime, only experiments can provide the flow data needed for any qualification of new flight hardware.

The centerline static pressure and Mach number are shown in Fig. 27. The static pressure behind the Mach disk is above ambient. The reflection point of the internal shock wave is visible in a pressure increase and a Mach number decrease. For $p_c/p_a = 125$, a small backflow region that can be associated with a small ring vortex is situated downstream of the Mach disk.

Comparison

Finally, results obtained with the different gas models are compared. The influence of the gas model on the wall pressure distribution is minimal (Fig. 28). Because at $p_c/p_a = 115.5$, the nozzle is full flowing the difference in the wall pressure distribution between

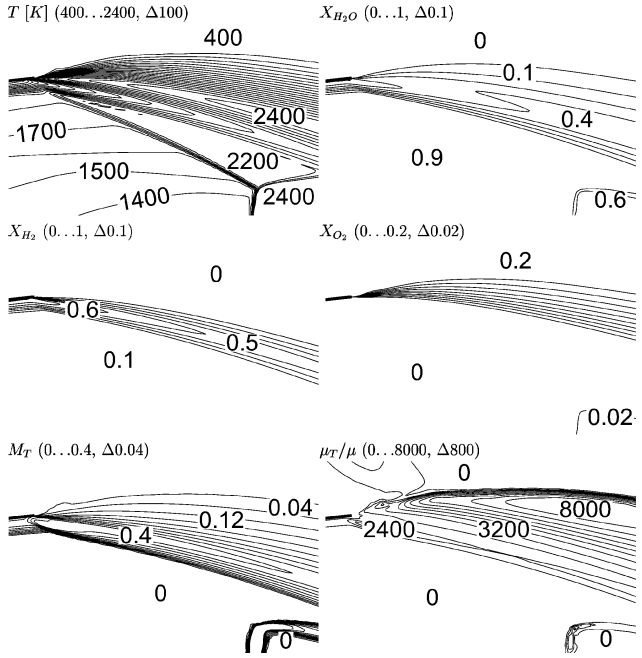

Fig. 22 Vulcain 2, finite rate chemistry, $p_c/p_a = 125$, close-ups at nozzle exit.

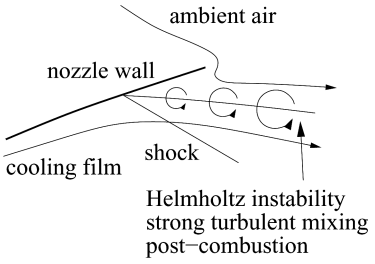

Fig. 23 Schematic view of postcombustion area at jet boundary.

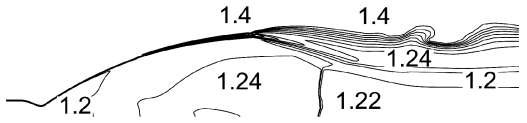

Fig. 24 Vulcain 2, finite rate chemistry, $p_c/p_a = 125$, ratio of specific heats γ (1.2, . . . , 1.4, Δ0.02).

FSS and RSS is negligible. Because of the cooling film, the wall temperatures predicted by the nonequilibrium computations are considerably below the wall temperatures predicted by the two other gas models. Also, as noted earlier, for the nonequilibrium model, the wall temperature rises in the separated flow region, possibly due to postcombustion of excess hydrogen. Comparing the perfect gas and the equilibrium chemistry model, one finds a lower predicted wall temperature for the latter. As mentioned in the discussion of the Vulcain results, a limited variation of the fuel mixture ratio O/F and the ratio of specific heats γ does not significantly alter the wall temperature distribution, but has great impact on the resulting shock patterns (FSS or RSS, cap shock or Mach disk).

Centerline distributions of static pressure, temperature, and Mach number are shown in Fig. 29. The RSS solution, which was obtained with the perfect-gas model and $\gamma = 1.16$, is noticeably different from all other cases, which show FSS. For RSS, the normal shock is positioned considerably upstream of the location where the Mach disk appears for FSS. Although the static pressure behind the normal shock is approximately the same for RSS as for FSS, it reaches a maximum of $p_{c1}/p_a \approx 6$ for RSS at the downstream end of the vortex ring. Correspondingly, the centerline temperature rises to a second plateau point at $x/r_{th} \approx 35$. The strength of the vortex ring may be deduced from the maximum centerline reverse flow Mach

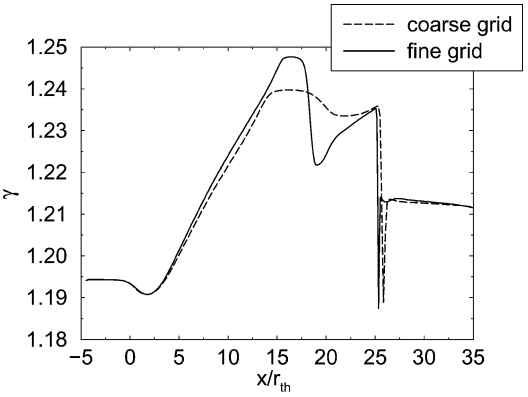

Fig. 25 Vulcain 2, finite rate chemistry, $p_c/p_a = 125$, centerline ratio of specific heats γ.

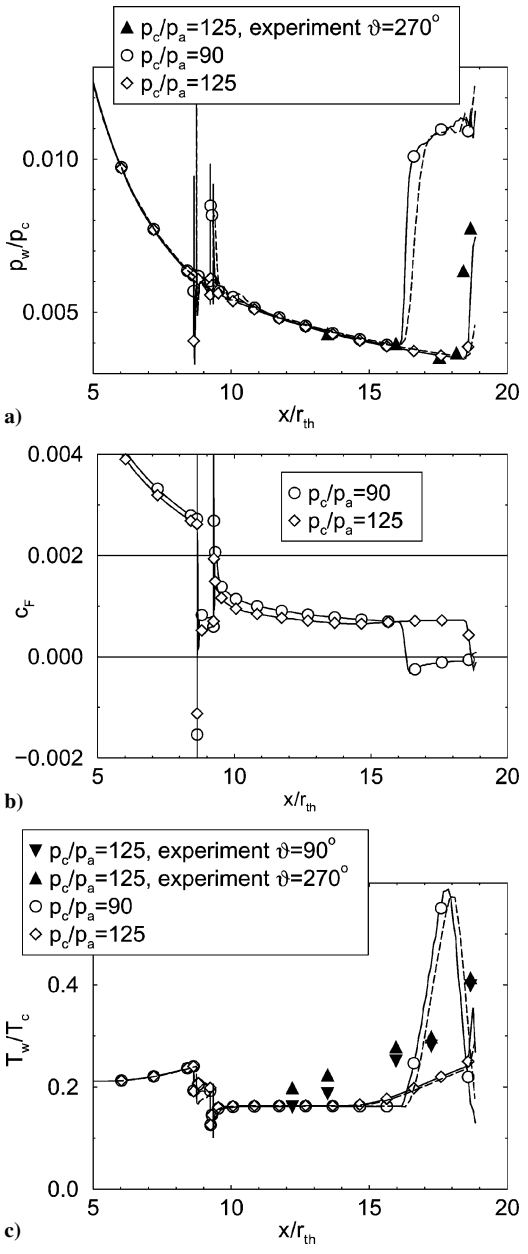

Fig. 26 Vulcain 2, finite rate chemistry: a) wall pressure, b) skin-friction coefficient, and c) wall temperature; ——, fine grid results and – – –, coarse grid results.

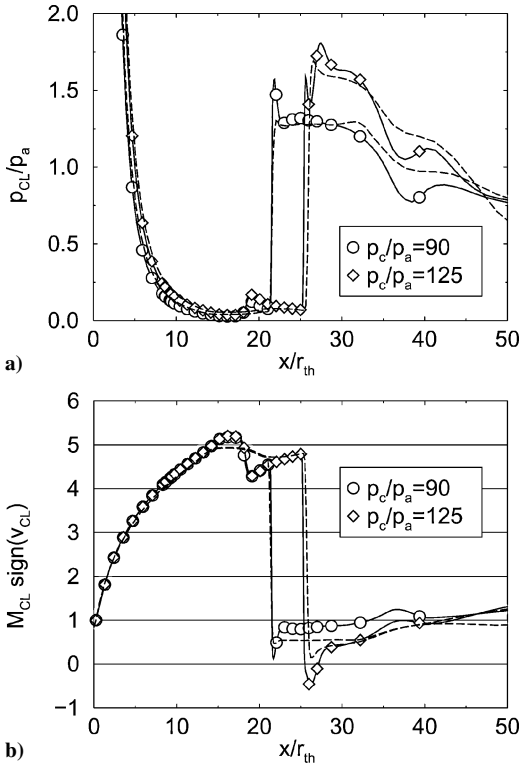

Fig. 27 Vulcain 2, finite rate chemistry: a) centerline pressure and b) Mach number; ——, fine grid results and – – –, coarse grid results.

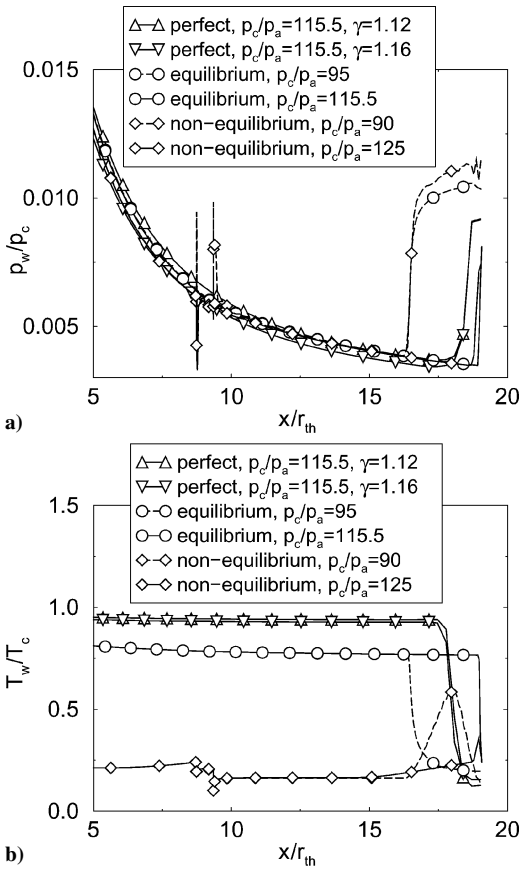

Fig. 28 Vulcain 2 and Vulcain 2 clean, comparison of a) computed wall pressures and b) temperatures.

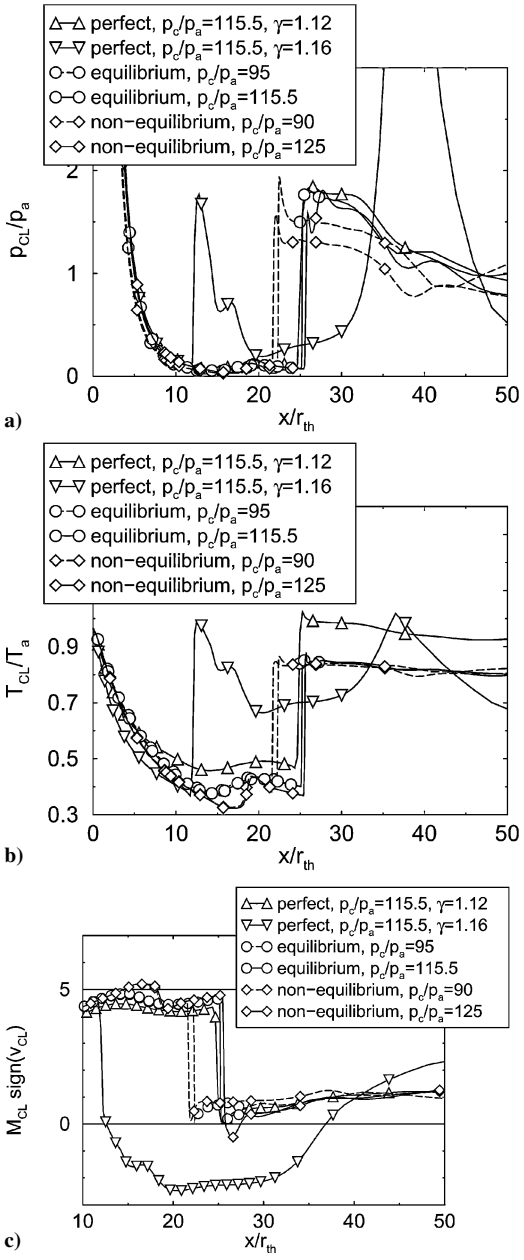

Fig. 29 Vulcain 2 and Vulcain 2 clean, comparison of a) computed centerline pressures, b) temperatures, and c) Mach numbers.

number of ≈2. However, downstream grid stretching was used for $x/r_{\text{th}} \geq 30$, and the RSS result may, therefore, serve as a qualitative reference only. Otherwise, independent of the respective gas model used, the location of the strong normal shock is predicted for approximately the same location for $p_c/p_a = 95$ and 90 (equilibrium and nonequilibrium solution) and $p_c/p_a = 115.5$ and 125 (perfect gas with $\gamma = 1.12$, equilibrium, and nonequilibrium solution). Centerline static pressure, temperature, and Mach number ahead and behind the shock are about the same. The only noticeable differences between the various results are the resolution of the reflection point of the internal shock wave at $x/r_{\text{th}} \approx 18$ and the postcombustion discussed earlier.

The comparison illustrates how the use of gas models more elaborate than the perfect-gas model (with adjusted ratio of specific heats) is only justified when wall temperature predictions have to be made, when the gas composition varies, and when combustion processes play a role. Nevertheless, because uncertainty is involved when a proper γ value is selected, the equilibrium-gas model should be chosen over the perfect-gas model.

Conclusions

A numerical method for the simulation of hot gas nozzle flows was presented. Simulations of the Vulcain and the Vulcain 2 rocket engine nozzles were performed with three different gas models: the perfect-gas model, the chemical equilibrium model, and the chemical non-equilibrium model.

For Vulcain RSS and FSS were shown in equilibrium-gas computations. For Vulcain 2, the importance of the ratio of specific heats for the appearance of either RSS or FSS was demonstrated in perfect-gas simulations. The comparison of an equilibrium computation and a chemical nonequilibrium computation revealed the existence of a postcombustion area in the shear layer where the hydrogen-rich nozzle gas comes into contact with the ambient air.

Because it became apparent that some of the assumptions made in this paper, for example, the steady flow assumption, prohibit the correct quantitative prediction of important physical processes, such as the break-down of the cooling film, care should be taken if the computations are used for qualitative predictions. The separated flow region is dominated by strong shear layers and, hence, strong instability mechanisms. The cooling film inside the nozzle does also feature a distinct shear layer. The correct simulation of the turbulent mixing processes in these shear layers appears to be a prerequisite for the quantitative prediction of combustion phenomena and heat loads.

Acknowledgments

This work was supported in part by the German National Technology Program on Cryogenic Engine Research and the European Flow Separation Control Device technology programs. The authors wish to thank the various people involved in both programs for their cooperation, helpful discussions, and support.

References

[1]Nave, L. H., and Coffey, G. A., "Sea Level Side Loads in High-Area-Ratio Rocket Engines," AIAA Paper 73-1284, Nov. 1973.

[2]Frey, M., and Hagemann, G., "Flow Separation and Side-Loads in Rocket Nozzles," AIAA Paper 99-2815, June 1999.

[3]Chen, C. L., Chakravarthy, S. R., and Hung, C. M., "Numerical Investigation of Separated Nozzle Flows," *AIAA Journal*, Vol. 32, No. 9, 1994, pp. 1836–1843.

[4]Nasuti, F., and Onofri, M., "Viscous and Inviscid Vortex Generation During Nozzle Flow Transients," *AIAA Journal*, Vol. 36, No. 5, 1998, pp. 809–815.

[5]Mattsson, J., Högmann, U., and Torngren, L., "A Subscale Test Program on Investigation of Flow Separation and Sideloads in Rocket Nozzles," *Proceedings of the 3rd European Symposium on Aerothermodynamics for Space Vehicles*, ESA–European Space Research and Technology Centre ESA Publications Division, ESTEC, Noordwijk, The Netherlands, 1999, pp. 373–378.

[6]Hunter, C. A., "Experimental, Theoretical, and Computational Investigation of Separated Nozzle Flows," AIAA Paper 98-3107, July 1998.

[7]Dougherty, N. S., and Liu, B.L., "Navier–Stokes Computations with Finite-Rate Chemistry for LO_2/LH_2 Rocket Engine Plume Flow Studies," AIAA Paper 91-0246, Jan. 1991.

[8]Schröder, W., and Hartmann, G., "Implicit Solutions of Three-Dimensional Viscous Hypersonic Flows," *Computer and Fluids*, Vol. 21, No. 1, 1992, pp. 109–132.

[9]Knab, O., and Weiland, C., "Effect of Detailed Physical–Chemical Modeling on Film-Cooled Nozzle Flow Calculations," AIAA Paper 97-2910, July 1997.

[10]Terhardt, M., Hagemann, G., and Frey, M., "Flow Separation and Side-Load Behavior of the Vulcain Engine," AIAA Paper 99-2762, June 1999.

[11]Caisso, P., Brossel, P., and Souchier, A., "Development Status of the Vulcain 2 Engine," AIAA Paper 2002-3840, July 2002.

[12]Nietubicz, C. J., Pulliam, T. H., and Steger, J. L., "Numerical Solution of the Azimuthal-Invariant Thin-Layer Navier–Stokes Equations," *AIAA Journal*, Vol. 18, No. 12, 1980, pp. 1411–1412.

[13]Wilcox, D. C., "Turbulence Modeling for CFD," DCW Industries, La Cañada, CA, 1993.

[14]Wilcox, D. C., "Progress in Hypersonic Turbulence Modeling," AIAA Paper 91-1785, June 1991.

[15]Anderson, J. D., "Hypersonic and High Temperature Gas Dynamics," McGraw–Hill, New York, 1989.

[16]Gordon, S., and McBride, B. J., "Computer Program for Calculation of Complex Chemical Equilibrium Compositions, Rocket Performance, Incident and Reflected Shocks, and Chapman–Jouguet Detonations," NASA SP-273, 1971.

[17]Svehla, R. A., and McBride, B. J., "Fortran IV Computer Program for Calculation of Thermodynamic and Transport Properties of Complex Chemical Systems," NASA TN D-7056, 1973.

[18]Gross, A., "Numerische Untersuchung Abgelöster Düsenströmungen," Ph.D. Dissertation, Rheinisch-Westfälische Technische Hochschule Aachen, Aachen, Germany, 2002.

[19]Maas, U., and Pope, S. B., "Simplifying Chemical Kinetics: Intrinsic Low-Dimensional Manifolds in Composition Space," *Combustion and Flame*, Vol. 88, Nos. 3, 4, 1992, pp. 239–264.

[20]Giles, M. B., "Nonreflecting Boundary Conditions for Euler Equation Calculations," *AIAA Journal*, Vol. 28, No. 12, 1990, pp. 2050–2058.

[21]Gross, A., and Weiland, C., "Investigation of Shock Patterns and Separation Behavior of Several Subscale Nozzles," AIAA Paper 2000-3293, July 2000.

[22]Gross, A., Haidn, O., Stark, R., Zeiss, W., Weber, C., and Weiland, C., "Experimental and Numerical Investigation of Heat Loads in Separated Nozzle Flow," AIAA Paper 2001-3682, July 2001.

[23]Roe, P. L., "Approximate Riemann Solvers, Parameter Vectors, and Difference Schemes," *Journal of Computational Physics*, Vol. 43, No. 2, 1981, pp. 357–372.

[24]Yee, H. C., "Upwind and Symmetric Shock-Capturing Schemes," NASA TM 89464, May 1987.

[25]Yee, H. C., and Harten, A., "Implicit TVD Schemes for Hyperbolic Conservation Laws in Curvilinear Coordinates," *AIAA Journal*, Vol. 25, No. 2, 1987, pp. 266–274.

[26]Rossow, C.-C., "A Flux Splitting Scheme for Compressible and Incompressible Flows," *Journal of Computational Physics*, Vol. 164, No. 1, 2000, pp. 104–122.

[27]Schröder, W., and Mergler, F., "Investigation of the Flowfield over Parallel-Arranged Launch Vehicles," AIAA Paper 93-3060, July 1993.

[28]Weber, C., Behr, R., and Weiland, C., "Investigation of Hypersonic Turbulent Flow over the X-38 Crew Return Vehicle," AIAA Paper 2000-2601, June 2000.

[29]Larrouturou, B., "How to Preserve the Mass Fractions Positivity when Computing Compressible Multicomponent Flows," *Journal of Computational Physics*, Vol. 95, No. 1, 1991, pp. 59–84.

[30]Frey, M., "Shock Patterns in the Plume of Overexpanded Nozzles," *Proceedings of the 3rd European Symposium on Aerothermodynamics for Space Vehicles*, ESA–European Space Research and Technology Centre ESA Publications Division, ESTEC, Noordwijk, The Netherlands, 1999, pp. 395–402.